











Basic Research

A Novel Nanostructured Surface on Titanium Implants Increases Osseointegration in a Sheep Model

Claire F. Jones PhD^{1,2}, Ryan D. Quarrington PhD¹, Helen Tsangari BSc³, Yolandi Starczak PhD¹, Adnan Mulaibrahimovic BSc¹, Anouck L. S. Burzava PhD^{4,5}, Chris Christou BVSc, PhD⁶, Alex J. Barker PhD³, James Morel BE⁷, Richard Bright MSc^{4,5}, Dan Barker PhD⁷, Toby Brown PhD⁷, Krasimir Vasilev PhD^{4,5}, Paul H. Anderson PhD^{3,5}

Received: 16 December 2021 / Accepted: 28 June 2022 / Published online: 24 August 2022
Copyright © 2022 by the Association of Bone and Joint Surgeons

Abstract

Background A nanostructured titanium surface that promotes antimicrobial activity and osseointegration would provide the opportunity to create medical implants that can prevent orthopaedic infection and improve bone integration. Although nanostructured surfaces can exhibit antimicrobial activity, it is not known whether these surfaces are safe and conducive to osseointegration.

Questions/purposes Using a sheep animal model, we sought to determine whether the bony integration of medical-grade, titanium, porous-coated implants with a unique nanostructured surface modification (alkaline heat treatment [AHT]) previously shown to kill bacteria was better than that for a clinically accepted control surface of porous-coated titanium covered with hydroxyapatite (PCHA) after 12 weeks in vivo. The null hypothesis was

that there would be no difference between implants with respect to the primary outcomes: interfacial shear strength and percent intersection surface (the percentage of implant surface with bone contact, as defined by a micro-CT protocol), and the secondary outcomes: stiffness, peak load, energy to failure, and micro-CT (bone volume/total volume [BV/TV], trabecular thickness [Tb.Th], and trabecular number [Tb.N]) and histomorphometric (bone-implant contact [BIC]) parameters.

Methods Implants of each material (alkaline heat-treated and hydroxyapatite-coated titanium) were surgically inserted into femoral and tibial metaphyseal cancellous bone (16 per implant type; interference fit) and in tibial cortices at three diaphyseal locations (24 per implant type; line-to-line fit) in eight skeletally mature sheep. At 12 weeks postoperatively,

The institutions of one or more of the authors (CFJ, KV, PHA) have received, during the study period, funding from the Innovative Manufacturing Co-operative Research Centre (IMCRC) grant (IMCRC/GOT/130318), which is co-funded by the Department of Industry, Science, Energy and Resources (Innovative Manufacturing CRC Ltd), Global Orthopaedic Technology Pty Ltd, The University of Adelaide, and The University of South Australia. The institutions of one or more of the authors (CFJ, KV, PHA) have received, during the study period, in-kind support from Global Orthopaedic Technology Pty Ltd, and Corin Australia.

One of the authors (DB) certifies receipt of personal payments or benefits, during the study period, in an amount of USD 10,000 to USD 100,000 from Corin Australia. One author (DB) was an employee of Global Orthopaedic Technology Pty Ltd. Two authors (JM, TB) were employees of Global Orthopaedic Technology Pty Ltd, and then Corin Australia.

All ICMJE Conflict of Interest Forms for authors and *Clinical Orthopaedics and Related Research*® editors and board members are on file with the publication and can be viewed on request.

Clinical Orthopaedics and Related Research® neither advocates nor endorses the use of any treatment, drug, or device. Readers are encouraged to always seek additional information, including FDA approval status, of any drug or device before clinical use.

Ethical approval for this study was obtained from the South Australian Health and Medical Research Institute Animal Ethics Committee (SAM366).

This work was performed at the South Australian Health and Medical Research Institute Pre-clinical Imaging and Research Laboratory, Adelaide, Australia; The University of Adelaide Medical School, Adelaide, Australia; and the UniSA Future Industries Institute, Adelaide, Australia.

bones were excised to assess osseointegration of AHT and PCHA implants via biomechanical push-through tests, micro-CT, and histomorphometry. Bone composition and remodeling patterns in adult sheep are similar to that of humans, and this model enables comparison of implants with ex vivo outcomes that are not permissible with humans. Comparisons of primary and secondary outcomes were undertaken with linear mixed-effects models that were developed for the cortical and cancellous groups separately and that included a random effect of animals, covariates to adjust for preoperative bodyweight, and implant location (left/right limb, femoral/tibial cancellous, cortical diaphyseal region, and medial/lateral cortex) as appropriate. Significance was set at an alpha of 0.05.

Results The estimated marginal mean interfacial shear strength for cancellous bone, adjusted for covariates, was 1.6 MPa greater for AHT implants (9.3 MPa) than for PCHA implants (7.7 MPa) (95% CI 0.5 to 2.8; $p = 0.006$). Similarly, the estimated marginal mean interfacial shear strength for cortical bone, adjusted for covariates, was 6.6 MPa greater for AHT implants (25.5 MPa) than for PCHA implants (18.9 MPa) (95% CI 5.0 to 8.1; $p < 0.001$). No difference in the implant-bone percent intersection surface was detected for cancellous sites (cancellous AHT 55.1% and PCHA 58.7%; adjusted difference of estimated marginal mean -3.6% [95% CI -8.1% to 0.9%]; $p = 0.11$). In cortical bone, the estimated marginal mean percent intersection surface at the medial site, adjusted for covariates, was 11.8% higher for AHT implants (58.1%) than for PCHA (46.2% [95% CI 7.1% to 16.6%]; $p < 0.001$) and was not different at the lateral site (AHT 75.8% and PCHA 74.9%; adjusted difference of estimated marginal mean 0.9% [95% CI -3.8% to 5.7%]; $p = 0.70$).

Conclusion These data suggest there is stronger integration of bone on the AHT surface than on the PCHA surface at 12 weeks postimplantation in this sheep model.

Clinical Relevance Given that the AHT implants formed a more robust interface with cortical and cancellous bone than

the PCHA implants, a clinical noninferiority study using hip stems with identical geometries can now be performed to compare the same surfaces used in this study. The results of this preclinical study provide an ethical baseline to proceed with such a clinical study given the potential of the alkaline heat-treated surface to reduce periprosthetic joint infection and enhance implant osseointegration.

Introduction

Titanium and its alloys are preferred biomaterials for orthopaedic applications because of their favorable corrosion resistance, biocompatibility, high strength-to-weight-ratio, ductility, and an elastic modulus closer to that of cortical bone compared with cobalt-chrome-molybdenum alloys or 316L stainless steel [34, 35, 62, 68, 74]. Titanium and its surface modification have been shown to stimulate osteoblast proliferation and to encourage osseointegration [80, 91, 94]. The mainstays of surface modification of the intraosseous region of orthopaedic implants have been coatings of porous, commercially pure titanium, hydroxyapatite, or a combination of the two [45, 55, 62, 77, 85]. Despite the demonstrated application of these surface modifications in orthopaedic devices, challenges persist, including infection [51, 72], aseptic loosening [9, 51], delamination, and loss of hydroxyapatite [29, 86]. Alternative titanium surface modifications have been proposed to address these challenges, including surfaces achieved by chemical vapor deposition [38], sol-gel methods [41], anodization [47], electrodeposition [61], microarc oxidation [79], acid etching [42], and alkaline heat treatments [43].

Alkaline heat-treated titanium surfaces have particularly shown potential to improve osseointegration and prevent the colonization of bacteria [14, 17, 43, 48, 52, 53, 63]. Recently, we examined the potential of an alkaline heat-treated surface to resist bacterial infection in vitro [15, 16]. We used hydrothermal etching to create a spike-like, nanostructured surface

¹Centre for Orthopaedic and Trauma Research, Adelaide Medical School, The University of Adelaide, Adelaide, Australia

²School of Mechanical Engineering, The University of Adelaide, Adelaide, Australia

³Health and Biomedical Innovation, Clinical and Health Sciences, University of South Australia, Adelaide, Australia

⁴STEM, University of South Australia, Adelaide, Australia

⁵Future Industries Institute, University of South Australia, Adelaide, Australia

⁶Preclinical, Imaging and Research Laboratories, South Australian Health and Medical Research Institute, Adelaide, Australia

⁷Corin Australia, Pymble, Australia

C. F. Jones ✉, Level 7, Adelaide Health and Medical Sciences Building, The University of Adelaide, North Terrace, Adelaide, South Australia 5005, Australia, Email: claire.jones@adelaide.edu.au

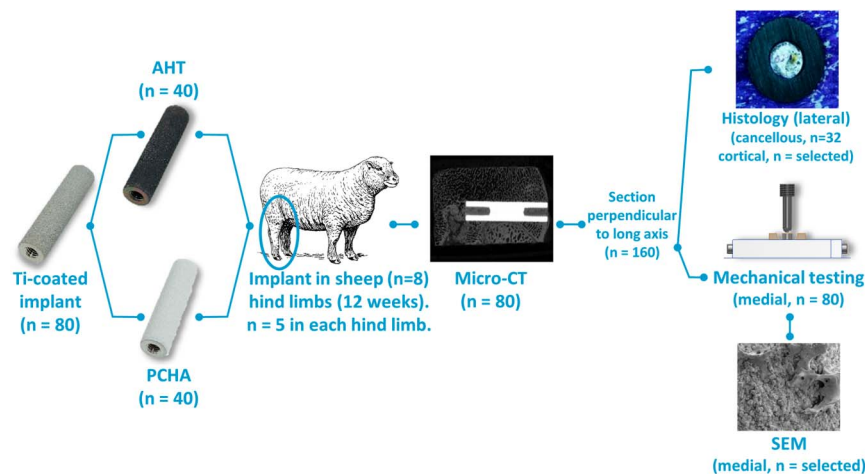


Fig. 1 An overview of the study design, with implant and specimen numbers for each process, is shown.

topography on a polished medical-grade titanium alloy, with the resulting surface demonstrating reductions in the viability of adhered bacteria. To determine whether a spike-like, nanostructured surface can be used in patients, it is important to confirm that the surface exhibits equal or improved osteogenic potential compared with current gold-standard clinically available implant surfaces.

Therefore, we sought to compare the osseointegration of an alkaline heat-treated (AHT) surface on a titanium porous coating with the clinically accepted control surface of Ti porous coating combined with hydroxyapatite after 12 weeks in vivo using cylindrical implants in a sheep tibial cortex [11, 27, 82-84, 89] and femoral and tibial epiphysis cancellous bone model [12, 88, 89]. The null hypothesis was that there would be no difference between implants with respect to the primary outcomes: interfacial shear strength and percent intersection surface (the proportion of implant surface area in contact with bone mineral), and the secondary outcomes: stiffness, peak load, energy to failure, and micro-CT (bone volume/total volume [BV/TV], trabecular thickness [Tb.Th], trabecular number [Tb.N]) and histomorphometric (bone-implant contact [BIC]) parameters.

Materials and Methods

Overview of Study Design

To evaluate osseointegration, cylindrical dowels of titanium alloy were porous-coated with commercially pure titanium and either surface-modified with alkaline heat treatment or coated with hydroxyapatite (Fig. 1) and then implanted at five cortical and cancellous sites in both hindlimbs of skeletally mature sheep for 12 weeks (Fig. 2). Porous commercially pure titanium coated with hydroxyapatite (PCHA) is a

common surface for uncemented titanium orthopaedic implants [28]. The sheep long bone model has been used extensively for similar evaluations of osseointegration [11-13, 18, 19, 26, 84, 87]. Although limited direct comparisons can be made between the surgical, loading, kinematic, and pathological environment of this long bone ongrowth model and of human implants, this model allows examination of bone response and the resulting bone-implant interface beyond that possible in human studies, namely with micro-CT, histology, and mechanical testing. The implants were subsequently harvested for histologic, micro-CT, and biomechanical analyses (Fig. 1). To assess BIC and the microstructure of the cancellous bone adjacent to the implant, harvested bone-implant specimens were evaluated for bone intersection surface, BV/TV, Tb.Th, and Tb.N using micro-CT. Each implant was then cut in half, perpendicular to the long axis. To assess BIC, histologic specimens were prepared for each lateral cancellous specimen and representative lateral cortical specimens. To assess the mechanical integrity of the bone-implant interface, medial specimens underwent “push-out” mechanical testing to measure the strength of the bone-implant interface, bone-implant construct stiffness, failure and peak load, and energy to failure. To visually assess post-implantation alkaline heat-treated surface morphology and osseointegration, selected specimens were viewed with scanning electron microscopy (SEM) after mechanical testing.

Implant Preparation and Characterization Before Implantation

To prepare the AHT implants, Ti-6Al-4V [4] cylinders (length: 25 mm; diameter: 5.7 mm; 6-mm-deep M3 thread at each end) were plasma spray-coated with unalloyed

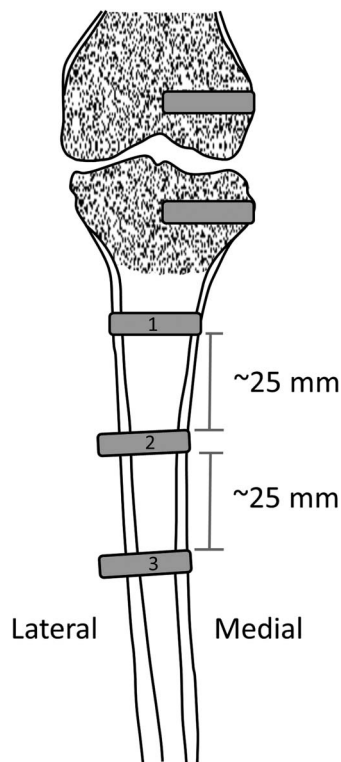


Fig. 2 The position of implants in the sheep femoral and tibial cancellous and cortical bone is shown.

titanium ASTM F67 Grade 2 (commercially pure titanium) to create a porous coating [3]. These implants were hydrothermally etched in a stainless steel reactor (Parr Instrument Company) using a 1M KOH aqueous solution followed by heat treatment in a furnace, as previously described [16], to create the nanostructured surface. To prepare the control PCHA implants, Ti-6Al-4V cylinders with an identical substrate diameter were plasma spray-coated with commercially pure titanium and coated with hydroxyapatite [5]. The PCHA surface was prepared using a commercial process identical to that used on the Paragon™ stem (Corin Pty Ltd). The final implant diameter was 6 mm (+0.16, -0.08) for both implant types.

SEM was used to characterize the AHT and PCHA implant surface topographies before implantation. Implant samples were imaged using a ZEISS “Merlin” SEM (Oberkochen) equipped with a Gemini II field emission gun column and operated at 2 kV with secondary and/or in-lens detectors at magnifications ranging from 5000× to 50,000×. Substrate surfaces were oriented in the SEM at 45° relative to the horizontal plane, and an oblique view revealed additional information about implant nanotopography that could not be assessed from a top-down perspective. SEM imaging confirmed that the AHT implants were uniformly covered in nanospine structures before implantation (Fig. 3), and the PCHA implant surface

was characterized by a microcrystalline topography because of the application of hydroxyapatite on the plasma-sprayed titanium coating (Fig. 4).

X-ray photoelectron spectroscopy (XPS) was used to verify the chemical composition of the porous-coated titanium surface of the AHT implant before and after alkaline heat treatment, as well as that of the PCHA implant surface, with one sample per type. Using an AXIS Ultra delay-line detector spectrometer (Kratos Analytical), we acquired spectra with a monochromatic Al K α radiation source operated at 15 keV and 15 mA. The survey spectra were recorded from a range of 0 eV to 1100 eV with a pass energy of 160 eV at a resolution of 0.5 eV. High-resolution spectra were collected at 20 eV. Data processing and curve fitting were performed using Casa XPS software (CasaXPS), in which the binding energy of neutral C 1s was set at 285 eV in the survey spectra, and the binding energy of the Ti(IV) 2p $_{3/2}$ peak (TiO $_2$) was set at 458.6 eV in the high-resolution Ti 2p spectra.

The surface crystalline composition of commercially pure Ti was verified on three representative polished disc samples (height: 10 mm; diameter: 3 mm) before and after alkaline heat treatment using an Empyrean I Grazing angle X-ray diffraction (GAXRD) machine (Malvern Panalytical) equipped with a Cu K- α detector operated at 45 kV and 40 mA. Incident angles of 0.5°, 0.8°, 1.5°, and 2.5° were used to generate a crystallinity profile at four different depths between the surface and approaching 2 μ m deep for each sample, with a 2 θ range of 15° to 80°. A semiquantitative analysis was performed using HighScore Plus software (Malvern Panalytical) for phase identification coupled with peak fitting using the Pawley refinement method to ascertain the composition change with an increasing grazing angle and corresponding penetration depth.

The XPS analysis verified the commercially pure titanium porous coating before alkaline heat treatment processing (Supplementary Fig. 1; <http://links.lww.com/CORR/A889>). After alkaline heat treatment processing, an increase in oxygen content in the survey spectra and a shift toward a Ti $^{4+}$ oxidation state in the high-resolution Ti2p spectra were observed on the nanostructured surface, consistent with an increase in surface oxide layer thickness because of alkaline heat treatment processes [16]. Additionally, low levels of potassium were detected on the AHT surface, consistent with the use of potassium as the cation for the alkaline treatment. For the PCHA implants, XPS spectra verified the presence of elements, particularly calcium and phosphorus, consistent with hydroxyapatite coating on a PCHA surface used widely in orthopaedic implants (Supplementary Fig. 1B; <http://links.lww.com/CORR/A889>) [39, 76].

The GAXRD analysis provided further evidence of an increase in oxide layer thickness on commercially pure titanium because of alkaline heat treatment (Supplementary

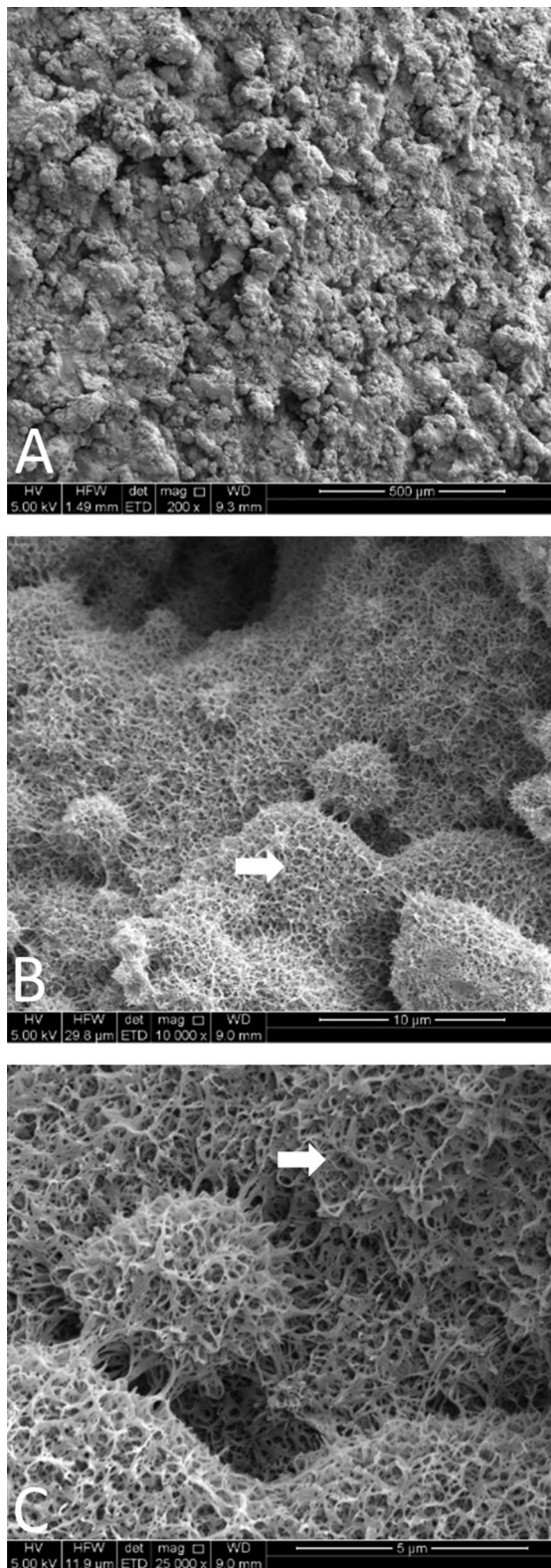


Fig. 3 A-C SEM images of alkaline heat-treated implants pre-implantation at magnifications of (A) 200 \times , (B) 10,000 \times , and (C) 25,000 \times , are shown. Spikes are visible on the surface of the implant preimplantation (white arrows).

Fig. 2; <http://links.lww.com/CORR/A890>). Before alkaline heat treatment, no titanium oxides were detected on samples; a typical oxide layer thickness of 3 to 7 nm was below the crystalline detection limits of the equipment [8, 75]. In contrast, at a grazing angle of 0.5°, the anatase crystalline phase of titanium dioxide was detected at a maximum concentration of 72% near the surface, decreasing to a consistent concentration of approximately 38% at a penetration depth of 1.7 μm .

Experimental Design and Animals

Eight skeletally mature Merino wether sheep (male, 18 to 24 months old, mean preoperative weight 65.8 ± 3.2 kg) were used for this study. Before inclusion in the study, all animals underwent a comprehensive physical assessment by a veterinary surgeon (CC); no animals were excluded from the study. Sheep were handled extensively for 3 weeks then acclimatized in pairs to their indoor pens for 7 days before surgery, to ensure quiet, calm, animals postoperatively. Preoperatively and postoperatively, animals were fed twice-daily rations of oaten hay, supplemented with lucerne chaff and oaten chaff, barley, and commercial sheep pellets (Lauke Mills). Sheep were fasted overnight (≥ 12 hours) before being anesthetized. South Australian mains water was provided ad libitum and was not withheld at any time. Animals were weighed on arrival at the facility, before surgery, and 6 and 12 weeks after surgery. All animals gained at least 30% bodyweight over the duration of the study.

Ten implants were implanted in the right and left hindlimb of each animal at two cancellous and three cortical locations per limb (Fig. 2). Sheep were randomly allocated to one of two groups defined by the limb receiving the test implants: for the first group, the right hindlimb received the control (PCHA) implants, and for the second group, the right hindlimb received the AHT implants. The random allocation sequence was generated using the `ralloc.ado` module, version 3.5.2, in Stata (version 15, Stata Corp) using a block size of four.

The sample size for this study was 24 implants per group in cortical sites and 16 implants per group in cancellous sites. An a priori power sample size estimate was performed for cortical interface shear strength, using G*Power software [37]. For a two-tailed difference between independent means, with an effect size of 0.83 (corresponding to a 5-MPa difference between groups, which was considered a meaningful difference, and an SD of 6 MPa corresponding to that typically observed for interface shear stress across various implant types in the cortical model) (Supplementary Table 1; <http://links.lww.com/CORR/A891>), power of 0.8 (β error 20%), and α of 0.05, the required sample size for each group was 24.

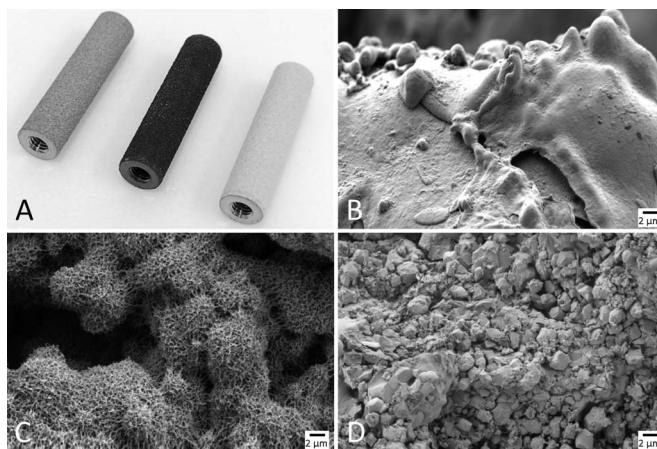


Fig. 4 (A) Photograph of sheep implants before implantation, from left to right: porous-coated titanium before alkaline heat treatment, after alkaline heat treatment, and PCHA; and SEM images demonstrating the nanotopographies and microtopographies of the same implants: (B) porous-coated titanium (before alkaline heat treatment), (C) alkaline heat-treated, and (D) PCHA. The SEM analysis demonstrates the change in nanosurface morphology on the porous plasma-sprayed coating before and after alkaline heat treatment processing, where the implant maintained the underlying microporous structure because of plasma-sprayed titanium. In contrast, the PCHA implant surface was characterized by a microcrystalline topography because of the application of hydroxyapatite on the plasma-sprayed titanium coating.

Surgical and Postoperative Procedures

A fentanyl patch (100 mg, 2 mcg/kg/hour) was placed on the right forelimb 24 hours preoperatively [27]. At the start of surgery, animals were sedated (diazepam 0.5 mg/kg; ketamine 8 mg/kg) and intubated, and anesthesia was maintained with isoflurane (1.5% to 3.5%) in oxygen (2 L/minute). Antibiotics were administered (long-acting benicillin 1 mL/10 kg intramuscular and long-acting oxytetracycline 200 mg/mL, 20 mg/kg), the fentanyl patch was renewed, and carprofen was administered (50 mg/mL and 4 mg/kg, intramuscular). Sheep were transferred to a surgical table and positioned in dorsal recumbency. Intravenous fluids (Hartmann solution) were given at 10 mL/kg/hour intraoperatively.

Incisions were made on the medial distal femoral condyles (10 mm long), proximal tibia (10 mm long), and proximal anteromedial tibial diaphysis (120 mm long, beginning 30 mm distal from the tibial plateau); the muscle was bluntly dissected; and the periosteum was dissected to expose the cortical bone surface. A circular defect was created at each location with a pneumatic drill with bit sizes of 4.5 mm and 5.7 mm (cancellous sites) to provide for a press (interference) fit and 4.5 mm and 6 mm (cortical sites) for a line-to-line fit (to maximize bone-implant contact while reducing risk of iatrogenic

fracture). Drilling, without saline irrigation, was performed in two stages to prevent buildup of heat from friction and thus thermal necrosis; a pilot hole was drilled with the 3-fluted 4.5-mm bit, then this was overdrilled with the 5.7-mm or 6-mm bit. The implant was seated by hand at each location and gently tapped in with a mallet, ensuring that the implant was nominally flush with the outer aspect of the medial cortex. At the cancellous sites, the deep muscular and tendinous tissues were closed with 0 Vicryl sutures, the subcutaneous layers with 3-0 Vicryl, and the skin with 2-0 Vicryl. At the cortical sites, the periosteum, soft tissue, and dermis were closed in layers using 3-0 Vicryl and 2-0 Polysorb, respectively. Postoperative survey craniomedial-caudolateral radiographs were obtained for each animal to assess implant positioning.

Animals then recovered from anesthesia and were housed indoors in individual recovery pens, with no weightbearing restrictions and with close monitoring for 2 weeks. Animals were then housed in covered outside pens in pairs for a further 2 weeks. At 4 weeks postoperatively, the animals were paddock housed as a flock for the final 8 weeks, with free access to pasture, supplemented as needed as described above. Animal observations were carried out at least once daily during these periods and recorded on their monitoring sheets.

All animals completed the 12-week observation period, and there were no postoperative complications, weight loss, or clinical infections.

At 12 weeks postoperatively, animals were humanely euthanized with sodium pentobarbitone (160 mg/kg intravenous). Once the tibia and femur were harvested and all soft tissue was removed, the tibia and femur were wrapped in phosphate-buffered saline (PBS)-soaked gauze and transported to the laboratory on ice. Limbs were sectioned into individual implant sites with a bandsaw, individually wrapped in PBS-soaked gauze, and stored at -20°C.

General Specimen Preparation

After thawing overnight at 4°C, the specimens underwent micro-CT scanning. High-resolution plain radiographs (LX-60 Cabinet X-ray System, Faxitron X-Ray LLC) were obtained in various views to establish the main axis of the implant in the specimen. Specimens were bisected orthogonally in the transverse plane using a low-speed saw (Model 660, South Bay Technology Inc; Diamond Wafering Blade, Diamond Resin Bond, 6" x 020" x 5"; Cat #. 60-20079, Buehler Ltd). This created 64 cancellous and 96 cortical specimens at least 12 mm long. Each medial specimen was then wrapped in PBS-soaked gauze and stored at -20°C before mechanical testing, and each lateral specimen was processed for histology.

Micro-CT

To assess contact between the implant and bone (bone intersection surface), and the microstructure of the cancellous bone adjacent to the implant, we obtained high-resolution micro-CT images for each specimen in air. Scan acquisition parameters were a resolution of 20.4- μm isotropic voxels, with each frame an average four images, and 580-ms exposure time (SkyScan 1276, Bruker). The X-ray filter was a 0.5-mm aluminium and 0.03-mm copper filter. The X-ray tube potential (peak) was 100 kVp, and the current was 200 μA . We reconstructed the images using nRecon software (version 1.7.3.1, Bruker), and we performed all analyses with CTAn software (v.1.17.7.2+, Bruker). Morphometric indices were determined using an adaptive thresholding algorithm with a prethresholding greyscale of 205 for bone and 250 for the implant, with a radius of eight pixels (163.2 μm) to only include bone (not the implant) and an outer radius of 20 pixels (408 μm) to determine the region of interest, as recommended by the manufacturer.

For the cancellous specimens, in the defined region of interest, BV/TV (%), Tb.Th, and Tb.N were determined. Percent intersection surface (i.S/TS; i.S – intersection surface [mm^2],

TS – total surface [mm^2]) analysis was performed on the length of cancellous implants (Supplementary Fig. 3A; <http://links.lww.com/CORR/A892>). For the cortical implants, the percent intersection surface analysis was performed only on the implant regions that were in contact with cortical bone (Supplementary Fig. 3B; <http://links.lww.com/CORR/A892>). Nomenclature and units were used in accordance with American Society of Bone and Mineral Research Histomorphometry Nomenclature Committee recommendations [31].

Histologic Specimen Preparation

Histologic specimens were prepared to measure BIC. Cortical and cancellous bone specimens were placed in 10% buffered formalin at room temperature for 5 days and dehydrated under vacuum in a desiccator (Pyrex desiccator, Cat# CLS3121200) (90% ethanol for 5 days and 2 \times changes of 100% ethanol for 4 days). Specimens were then placed in an infiltration solution of 100 mL methyl methacrylate (Cat# M55909, Sigma-Aldrich Inc) and 10 mL polyethylene glycol 400 (Cat# 8.07485, Sigma-Aldrich Inc) under vacuum in a desiccator at room temperature for 1 month, and then polymerized at 30°C using a solution of methyl methacrylate (100 mL), polyethylene glycol (10 mL), and perkadox (0.2%; organic peroxide CAS# 15520-11-3, AkzoNobel) for 1 week in a benchtop oven. Embedded resin samples were cut out of their containers, and excess resin was removed using a grinder/polisher (EcoMet30 Twin Semi-Automatic Grinder/Polisher, Buehler Ltd) with sandpaper grits of 60, 120, 400, and 800 until the surface of the bone and implant was reached. Thick sections (2 mm) were cut with a low-speed saw using a diamond wafering blade (Model 660 South Bay Technology). Sections were adhered to acrylic plastic sheets (150 mm x 50 mm, polycarbonate; Acrilix Plastics Pty Ltd) with two-part 24-hour epoxy resin (Araldite, Selleys), left to dry for 24 hours; ground to 200- μm thick using 120-grit, 400-grit, and 800-grit sandpaper; and polished with a polishing cloth and polishing solution (Masterprep polishing suspension of 0.05 μm , Buehler Ltd). Sections were then stained with 1% toluidine blue; briefly, sections were covered with 1% formic acid to etch the surface allowing for stain penetration (2 minutes), rinsed with distilled water (2 minutes), rinsed with 50% ethanol (2 minutes), rinsed with distilled water (2 minutes) and stained with 1% toluidine blue stain (5 minutes), rinsed in distilled water, and dried. Sections were imaged using a stereomicroscope (Olympus SZ61, Olympus Australia Pty) with a digital camera (Olympus DP20, Olympus Australia Pty Ltd) at 1.5 \times and 0.67 \times magnification. For cancellous specimens, ImageJ software (Version 1.52p, National Institutes of Health [74]) was used to measure linear BIC around the circumference of the implant in one representative section. The BIC is

expressed as $BIC = BC/IL$, where bone contact (BC) is the length of direct contact between the implant profile and bone tissue, and interface length (IL) indicates the total length of the implant surface available for bone apposition [7].

Mechanical Testing

To evaluate the mechanical behavior of the bone-implant construct, we performed push-out tests to determine interfacial shear strength and secondary measures of stiffness, peak load, and energy to failure. Fresh-frozen specimens were defrosted at 4°C for approximately 24 hours before preparation and brought to room temperature. Any remaining soft or periosteal tissue or intramedullary fat was removed. Tissue growth over the medial cancellous implant surface was carefully removed with a Dremel burr to reveal the threaded hole for embedding alignment. Overlying bone was typically not fully mineralized and was easily removed. Premicro-CT and postmicro-CT of three specimens confirmed qualitatively that this procedure did not substantially alter bone and bone-implant micro-CT parameters, suggesting the process did not alter the bone-implant interface. A small portion of the contralateral endosteal surface of some cortical specimens was removed to facilitate access to the implant for embedding alignment.

Specimens were embedded in polymethyl methacrylate (PMMA) (Vertex Dental) using a custom jig to ensure vertical alignment of the implant and thereby minimize off-axis loading during push-through mechanical testing (Supplementary Fig. 4; <http://links.lww.com/CORR/A893>). For cortical specimens, the implant stub protruding into the intramedullary canal was gripped with an alignment cuff and fixed with set screws. For cancellous specimens, the alignment rod was attached to the implant using the implant's internal thread. The embedding jig was lowered using a linear bearing and locked with the bony mantle at an appropriate distance from the bottom of the mold. Plasticine was placed as required to eliminate PMMA flow to exclusion areas. PMMA was then poured to an appropriate level, ensuring that clearance between the specimen and edge of the hole in the mold was greater than 0.7 mm (approximately 1 mm in our protocol) [32]. The PMMA was cured at room temperature for a minimum of 30 minutes before testing.

The mold and specimen were fixed to the base of a material testing machine (Instron 8874, Instron). The actuator was fitted with a biaxial load cell (25 kN axial load capacity) that was used to control load limits during the test in series with a six-axis load cell (MC3A, AMTI; 4.4 kN axial load capacity). The actuator, which had a 5-mm-diameter loading pin with a hemispherical tip, was advanced downward at 0.5 mm/minute (displacement control) until the implant was completely expelled from the bone mantle.

Force-displacement data were acquired on the material testing machine's data acquisition system at 200 Hz. The six-axis load cell data and a synchronization pulse were acquired on a standalone data acquisition system (PXIe-1073, BNC-2120 & PXIe-4331, National Instruments) at 200 Hz.

Mechanical testing data were postprocessed using custom programs (R2015a, Matlab, Mathworks). Data were filtered (second-order, two-way Butterworth, low-pass cut-off frequency of 10 Hz). Off-axis (shear) load data were processed and are reported as a percentage of the peak load for each specimen. The following parameters were derived from the load-displacement relationships: linear region stiffness (slope of the linear region before failure; a measure of the elastic response of the bone-implant construct), peak load (the maximum load experienced before continual reduction in load, which corresponds to complete compromise of the interface which permits implant motion), and energy to failure (area under the load-displacement curve to the peak load; this is the energy required to compromise the bone-implant interface) (Supplementary Fig. 5; <http://links.lww.com/CORR/A894>). Interfacial shear stress was calculated by dividing the peak load by the bone-implant contact area (BICA). Peak load was used to calculate shear interface stress because this corresponded with initiation of gross implant motion within the bone. Interfacial shear stress is the primary mechanical outcome measure because it is normalized by the contact area at the bone-implant interface, thus accounting for the effect of geometric variability of the bone mantles.

We derived the BICA using specific custom protocols for cancellous and cortical specimens. For cancellous specimens, four measurements of the bone thickness were taken at 90° intervals around the circumference of the implant using digital Vernier calipers (500-196-30, Mitutoyo; resolution 0.01 mm). For the cortical specimens, we took measurements using micro-CT images acquired before mechanical testing (for specimens in which implant access was not affected by endosteal bone) or after mechanical testing (for specimens for which bone was removed to provide implant access, as described above). Images were imported into FIJI imaging software (ImageJ 1.51p), and bone thickness was measured using a virtual caliper tool at 30° increments around the implant's circumference. For both bone locations, physical or imaging measurements were imported into custom Matlab code (R2015a, Matlab, Mathworks) that calculated a plane of best fit representing the circumference of the bone-implant interface at either end of the implant, and BICA was calculated between these oblique planes. Before mechanical testing, all 32 cancellous specimens required clearance of bone overlying the implant thread; 14 of 48 cortical specimens required endosteal bone removal. One specimen in the PCHA group was eliminated from the mechanical testing analysis because there was a visible defect (a crack

with no visual evidence of healing, suggesting it occurred during specimen preparation) in the bone adjacent to the implant, and the load-displacement curve differed substantially from the rest of the cohort. One specimen in the AHT cancellous group had a small shallow gap in the bone-implant interface at the medial bone surface, which likely contributed to higher off-axis loads (Supplementary Fig. 6; <http://links.lww.com/CORR/A895>) but the load-displacement curve was not unusual. One specimen in the AHT group exceeded the six-axis load cell limit and was retested with the biaxial load cell alone.

Postimplantation Surface Characterization

After mechanical testing, we randomly chose several representative implants in which to visually assess the morphology of the AHT implant surface and the bone integration after 12 weeks in situ using SEM. Excess biological material was removed using the following method: Lipids were removed using 2% Triton-X wash for 1 hour in a 37°C oven and sonicated in solution for 10 minutes; implants were placed in 10% ethylenediaminetetraacetic acid and 10% sodium dodecyl sulfate in distilled, deionized water on a rocker at room temperature for 1 week; and implants were incubated for 72 hours in proteinase K at 55°C to remove as much integrated bone as possible. Implants were then sputter-coated with 3 µm of platinum. SEM images were captured using a FEI Quanta 450 field emission gun environmental SEM (Thermo Fisher Scientific Inc) operated at 5 kV with magnifications ranging from 5000× to 50,000×.

Primary and Secondary Study Outcomes

Our primary study goal was to compare interfacial shear strength and percent intersection surface of alkaline heat-treated and PCHA implants in cancellous and cortical bone. To assess interfacial shear strength, we performed push-out tests on explanted specimens and determined the interfacial shear strength from the peak load and the area of implant in contact with bone (BICA). To assess percent intersection surface, we performed micro-CT imaging and determined the area of the implant that was in contact with bone, normalized by the area available for contact.

Our secondary study goals were to compare the bone-implant construct stiffness, peak load, energy to failure, and linear BIC (histology, cancellous only) of AHT and PCHA implants in cancellous and cortical bone. Stiffness, peak load, and energy to failure were determined from the push-out test load-displacement curves. The BIC was manually segmented on digital images of representative histologic sections for each specimen.

Ethical Approval

All animal procedures were approved by the South Australian Health and Medical Research Institute Animal Ethics Committee (approval number SAM-366) and were performed in accordance with the National Health and Medical Research Council *Australian Code for the Care and Use of Animals for Scientific Purposes* (eighth edition, 2013 [updated 2021]) [67].

Statistical Analyses

We determined median and interquartile range for interfacial shear stress, percent intersection surface, stiffness, peak load, energy to failure, BV/TV, Tb.Th, Tb.N, and BIC. Multivariable linear mixed-effects models were used to estimate the effect of implant type on each micro-CT, histologic, and mechanical outcome of interest; models were developed for cortical and cancellous groups separately. All models included a priori covariates to control for the effects of implant location (left or right limb) and preoperative animal bodyweight. In models pertaining to cancellous specimens, an a priori covariate for femoral or tibial location was added, and in models pertaining to cortical specimens, an a priori covariate for the diaphyseal region of the implant (1, 2, 3) (Fig. 2) was added. For the model concerning percent intersection surface for cortical specimens, an a priori covariate for medial or lateral implant location was included, and a post hoc model incorporating the interaction of medial/lateral implant location with implant type was developed to determine whether the effect of implant type on percent intersection surface was dependent on medial/lateral location. Prescribed covariates were maintained in all models, regardless of their significance. For all models, a random intercept was specified to account for the dependency of repeated observations in individual animals. For each specimen type, the estimated marginal means for each outcome by implant type were estimated post hoc, with all other variables held at their mean values. All statistical analyses were performed using Stata (version 15, StataCorp). The level of statistical significance was set at 0.05. Complete linear mixed models for each cortical (Supplementary Table 2; <http://links.lww.com/CORR/A896>) and cancellous (Supplementary Table 3; <http://links.lww.com/CORR/A897>) outcome measure were recorded. Throughout the paper and supplementary material, when there is a discrepancy between the estimated means and their corresponding difference, this arises due to cumulative rounding error. The retained values reflect those corresponding to the confidence intervals presented.

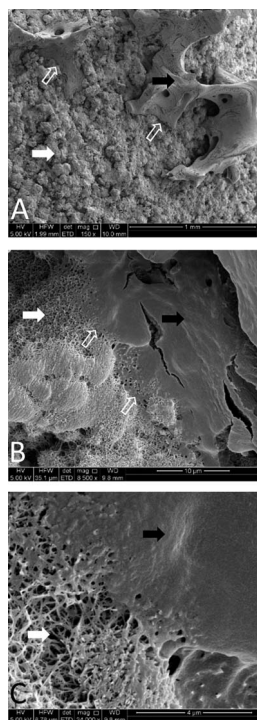


Fig. 5 A-C SEM images of alkaline heat-treated implants 12 weeks postoperatively at magnifications of (A) 150×, (B) 8500×, and (C) 34,000× are shown. Spikes are visible on the surface of the implant 12 weeks after implantation (white arrows); osseous material (black arrows) is evident and intimately associated with these spikes (open white arrows).

Results

SEM analyses of AHT implants from cancellous regions demonstrated that mineral was closely associated with the nanostructured surface of the implant (Fig. 5). Cancellous and cortical bone formed on the surface of AHT and PCHA implants (Fig. 6).

Interfacial Shear Strength

Our results showed that AHT implants exhibited a greater mean interfacial shear strength than did PCHA implants for both cancellous (adjusted estimated marginal mean 9.3 versus 7.7 MPa, adjusted estimated mean difference 1.6 MPa [95% CI 0.5 to 2.8 MPa]; $p = 0.006$) (Fig. 7A; Supplementary Table 3; <http://links.lww.com/CORR/A897>) and cortical (adjusted estimated marginal mean 25.5 versus 18.9 MPa, adjusted estimated mean difference 6.6 MPa [95% CI 5.0 to 8.1 MPa]; $p < 0.001$) (Fig. 7B; Supplementary Table 2; <http://links.lww.com/CORR/A896>) locations.

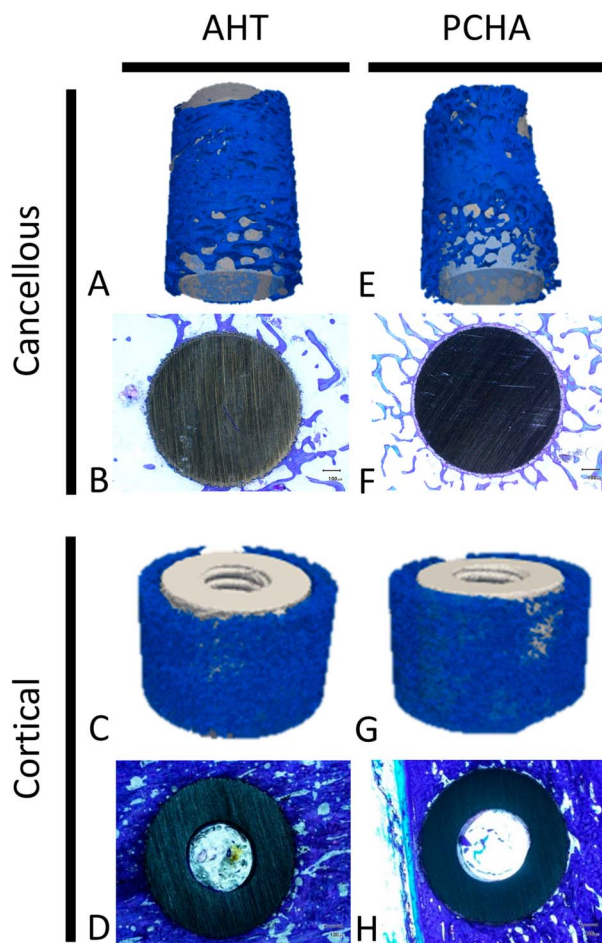


Fig. 6 Representative 3D-rendered reconstructions of micro-CT images of bone (blue) and representative two-dimensional toluidine blue–stained sections of bone (blue stain) surrounding AHT (left) and PCHA (right) implants in the cancellous and cortical bone regions are shown.

Percent Intersection Surface

We detected no difference in the implant-bone percent intersection surface for cancellous sites (adjusted estimated marginal mean 55.1% versus 58.7% for AHT and PCHA implants, respectively, adjusted estimated mean difference -3.6% [95% CI -8.1% to 0.9%]; $p = 0.11$) (Fig. 8A; Supplementary Table 3; <http://links.lww.com/CORR/A897>). In cortical bone, the percent intersection surface at the medial site was higher for the AHT than for the PCHA implants (adjusted estimated marginal mean 58.1% versus 46.2%, adjusted estimated mean difference 11.8% [95% CI 7.1% to 16.6%]; $p < 0.001$) (Fig. 8B) and not different for the lateral site (adjusted estimated marginal mean 75.8% versus 74.9%, adjusted estimated mean difference 0.9% [95% CI -3.8% to 5.7%]; $p = 0.70$) (Fig. 8C; Supplementary Table 2; <http://links.lww.com/CORR/A896>).

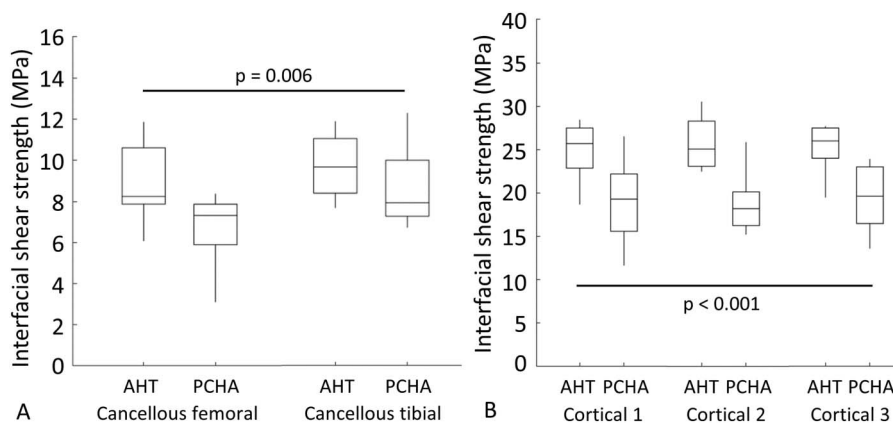


Fig. 7 A-B Descriptive statistics for interfacial shear strength for AHT and PCHA implants at the cancellous femoral and tibial locations are shown. In the box and whisker plots, the box's center line indicates the median value, the box's limits indicate the first (25th percentile) and third (75th percentile) quartiles, and the whiskers indicate the minimum and maximum values. The p values refer to the results of the corresponding linear mixed model.

Stiffness, Peak Load, and Energy to Failure

There was no difference in the implant-bone construct stiffness for cancellous locations (the adjusted estimated marginal mean for AHT implants was 3870 N/mm versus 3694 N/mm for PCHA implants, adjusted estimated mean difference 176 N/mm [95% CI -457 to 809 N/mm]; $p = 0.59$) (Fig. 9A; Supplementary Table 3; <http://links.lww.com/CORR/A897>) or cortical locations (the adjusted estimated marginal mean for AHT was 6920 N/mm versus 7062 N/mm for PCHA implants, adjusted estimated mean difference -141 N/mm [95% CI -701 to 418 N/mm]; $p = 0.62$) (Fig. 9B; Supplementary Table 2; <http://links.lww.com/CORR/A896>), adjusting for the effects of left versus right limb, location (femoral or tibial, diaphyseal region), and animal body weight. For cancellous sites, peak load was higher for the AHT implant (adjusted estimated marginal mean 2217 N) than for the PCHA implant (adjusted estimated marginal mean 1844 N), adjusting for the effects of left versus right limb, location (right/left, femoral/tibial), and animal body weight (adjusted estimated mean difference 373 N [95% CI 89 to 658 N]; $p = 0.01$) (Fig. 9C; Supplementary Table 3; <http://links.lww.com/CORR/A897>). Similar behavior was observed for peak load at cortical sites (the adjusted estimated marginal mean for AHT was 2746 N versus 2230 N for PCHA; adjusted estimated mean difference 516 N [95% CI 314 to 717 N]; $p < 0.001$) (Fig. 9D; Supplementary Table 2; <http://links.lww.com/CORR/A896>). Energy to failure was similar at cancellous sites (the adjusted estimated marginal mean for AHT implants was 1.12 J versus 0.75 J for PCHA; adjusted estimated mean difference 0.36 J [95% CI -0.02 to 0.74 J]; $p = 0.06$) (Fig. 9E; Supplementary Table 3; <http://links.lww.com/CORR/A897>), and greater for the AHT implant (adjusted estimated marginal mean 0.86 J) than the PCHA

implant (adjusted estimated marginal mean 0.51 J) at the cortical sites (adjusted estimated mean difference 0.35 J [95% CI 0.23 to 0.48 J]; $p < 0.001$) (Fig. 9F; Supplementary Table 2; <http://links.lww.com/CORR/A896>).

Bone-implant Contact

For the two-dimensional histomorphometry analyses of cancellous specimens, three of 32 sections were excluded: two PCHA femoral sections because of proximity to the growth plate and one PCHA tibial section because of technical difficulties with the resin embedding. For the remaining implants, the BIC was lower for the AHT implant (adjusted estimated marginal mean 35%) than the PCHA implant (adjusted estimated marginal mean 47%) after adjusting for implant location and animal body weight (adjusted estimated mean difference -12% [95% CI -19% to -4%]; $p = 0.002$) (Fig. 10; Supplementary Table 3; <http://links.lww.com/CORR/A897>).

BV/TV, Tb.Th, and Tb.N

For micro-CT analyses, five implants each for AHT and PCHA implants in the femur had a degree of growth plate encroachment, and two AHT implants and one PCHA implant in the tibia had growth plate encroachment. Despite this, all implants were included in the analyses. The BV/TV % of the cancellous bone surrounding the implant was similar for AHT and PCHA implants (the adjusted estimated marginal mean for the AHT implants was 45.5% versus 47.5% for the PCHA implants, adjusted estimated mean difference -1.9% [95% CI -6.0% to 2.2%]; $p = 0.36$), when

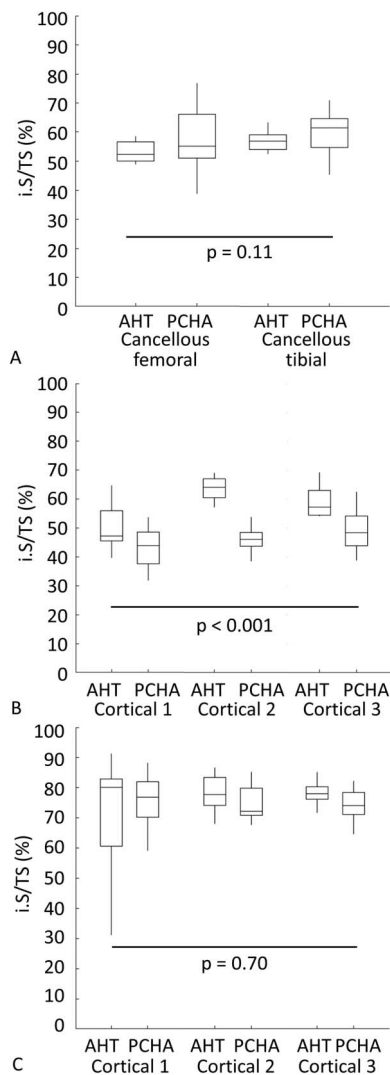


Fig. 8 A-C Descriptive statistics for percent intersection surface (i.S/TS; i.S – intersection surface [mm^2], TS – total surface [mm^2]) of bone on AHT and PCHA implants for (A) cancellous bone in the femur and tibia and for each location in the (B) medial and (C) lateral tibial cortex are shown. In the box and whisker plots, the box's center line indicates the median value, the box's limits indicate the first (25th percentile) and third (75th percentile) quartiles, and whiskers indicate the minimum and maximum values. The p values refer to the results of the corresponding linear mixed model.

adjusted for implant location (left/right limb, femoral/tibial) and bodyweight (Fig. 11A; Supplementary Table 3; <http://links.lww.com/CORR/A897>). We observed similar behavior for Tb.Th (the adjusted estimated marginal mean for AHT implants was 0.29 mm versus 0.31 mm for PCHA, adjusted estimated mean difference -0.02 mm [95% CI -0.05 to -0.002]; $p = 0.11$) (Fig. 11B; Supplementary Table 3; <http://links.lww.com/CORR/A897>) and Tb.N (the adjusted estimated marginal mean for AHT implants was 1.58 mm^{-1}

versus 1.52 mm^{-1} for PCHA, adjusted estimated mean difference 0.06 mm^{-1} [95% CI -0.05 to 0.17 mm^{-1}]; $p = 0.30$) (Fig. 11C; Supplementary Table 3; <http://links.lww.com/CORR/A897>).

Discussion

An optimal uncemented prosthesis surface should encourage rapid osseointegration and resist bacterial contamination. However, these two goals may be in conflict because the increased surface roughness and porosity that drives osseointegration can lead to an increase in bacterial attachment and colonization [92]. We previously demonstrated, in vitro, the capacity of a nanostructured surface to resist increasing concentrations of bacteria in contact with the implant surface [15, 16]. This spike-like, nanostructured surface topography was also shown to encourage increased mineralization in adhered osteoblasts [63]. This raised the exciting prospect that such a surface may have dual functionality in terms of encouraging rapid osseointegration and resisting bacterial contamination. In this study, the AHT implants exhibited a greater interface shear strength than the PCHA implants at the cancellous and cortical sites, consistent with increased strength of bone-implant integration for the AHT implant. The primary three-dimensional micro-CT outcome measure, percent intersection surface, was similar between the AHT and PCHA implants in cancellous sites, greater for the AHT implants in the medial cortex, but not different for implants in the lateral cortex. These findings, together with the previously reported antimicrobial properties [15, 16], offer potential for a next-generation uncemented orthopaedic implant surface. This is important given that prior attempts to increase osseointegration through increased roughening have led to enhanced opportunities for bacterial colonization [92].

Limitations

The model used in this study has some limitations. Although the sheep used were skeletally mature adults, they were nonetheless young, healthy animals with healthy bone healing responses. Their bone healing responses may differ from humans due to species, age, gender, loading, and pathological effects. Adult sheep are generally acknowledged to have bone composition, structure, and metabolism similar enough to humans to justify their use as a model in orthopaedic research, including osseointegration studies [64, 66, 69, 70], despite evidence of site-specific differences in bone density and Haversian remodeling [66, 71]. For example, in the context of osteoporosis models in female sheep, others have reported

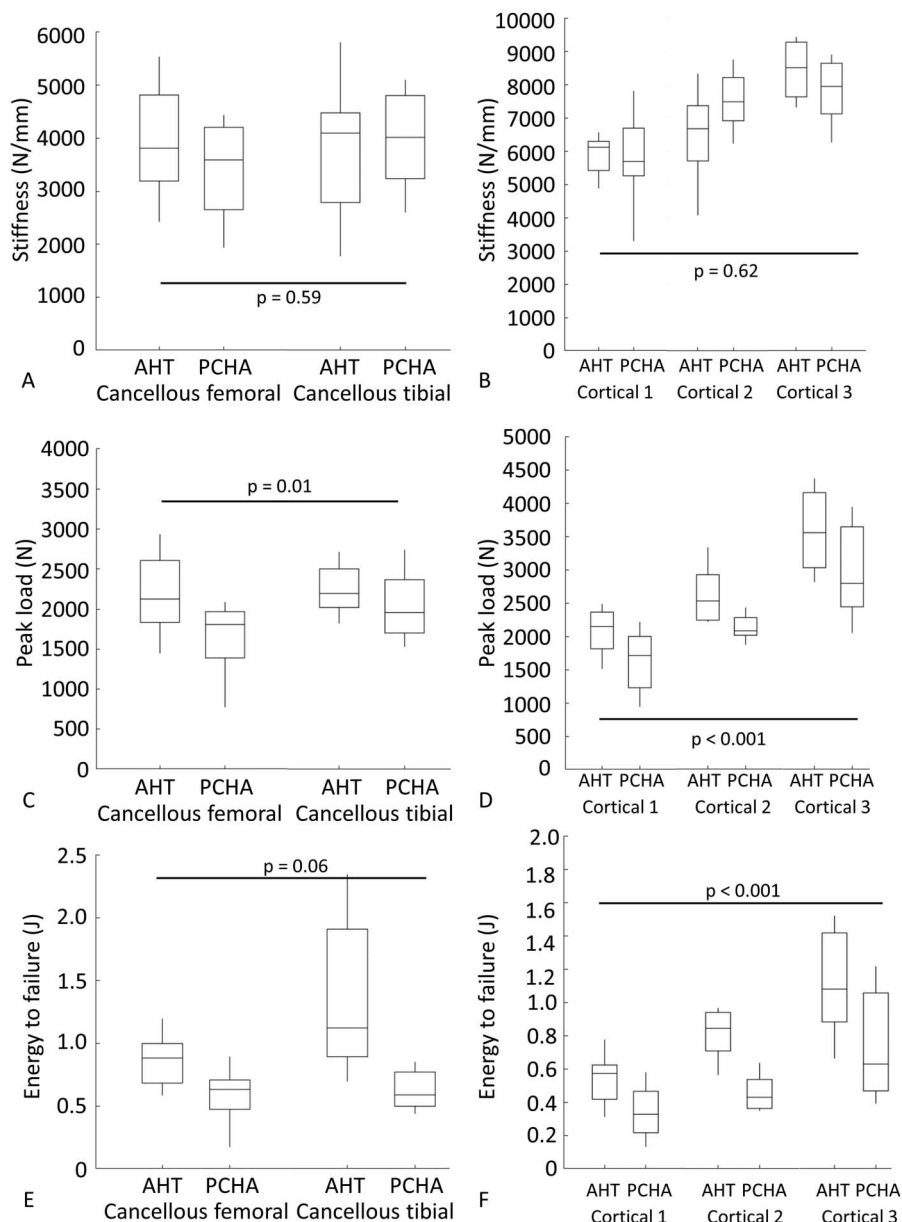


Fig. 9 A-F Descriptive statistics for mechanical testing outcomes for AHT and PCHA implants at the cancellous femoral and tibial locations and cortical locations are shown: (A) stiffness - cancellous, (B) stiffness - cortical, (C) peak load - cancellous, (D) peak load - cortical, (E) energy to failure - cancellous, and (F) energy to failure - cortical. In the box and whisker plots, the box's center line indicates the median value, the box's limits indicate the first (25th percentile) and third (75th percentile) quartiles, and the whiskers indicate the minimum and maximum values. The p values refer to the results of the corresponding linear mixed model.

similar bone responses to glucocorticoids [21, 25, 93], parathyroid hormone [30], bisphosphonates [30], fluoride [20, 23, 24], and selective estrogen receptor modulators [22] to those observed in humans; we are not aware of similar evidence in male sheep. A similar pattern and rate of mineral apposition, but a differing amount of bone in-

growth, has been observed in weightbearing implants inserted in the distal femoral condyle of sheep and humans [44, 90].

In this model, the implant was enclosed in a small standard defect and was not subjected to the complex loading that may be present in various orthopaedic

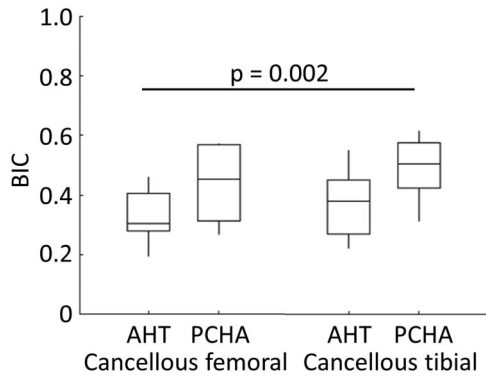


Fig. 10 Descriptive statistics for bone-implant contact for AHT and PCHA implants from cancellous femoral and tibial locations are shown. In the box and whisker plot, the box's center line indicates the median value, the box's limits indicate the first (25th percentile) and third (75th percentile) quartiles, and the whiskers indicate the minimum and maximum values. The p value refers to the result of the corresponding linear mixed model.

scenarios. Further, the implant had a uniform geometry and was relatively small compared with most human orthopaedic implants. However, this implant configuration allowed more implants to be assessed in a single animal, allowed within-subject comparison between the AHT and PCHA implants, and enabled reliable standardization to limit between-animal variability; all of these factors reduced the number of animals required to adequately power the study. Assessing osseointegration response with loading conditions and implant geometries that better represent the human implants to which the alkaline heat-treated surface treatment could be applied would be advantageous. We used only male (wether/castrated) sheep to minimize potential confounding effects of seasonal (hormonal) changes in bone metabolism that occur in female sheep [2], although to our knowledge, such seasonal variation has not been assessed in male sheep. It is not known whether osseointegration response to the AHT and PCHA implants would be different in females. In summary, although this sheep model cannot mimic all aspects of the human clinical scenario, it importantly limited animal-to-animal variation, allowed methods of assessment that are sensitive to differences in osseointegration, and evaluated the implant in cortical and cancellous bone tissue with bone remodeling responses similar to humans [66].

The clinical meaningfulness of the effect sizes observed in this study is not known, and we cannot be certain that similar effects or effect sizes would be observed in humans. However, for the reasons outlined above, the sheep long bone model is a biologically appropriate, relatively rapid, and cost-effective method to provide reasonable evidence for further

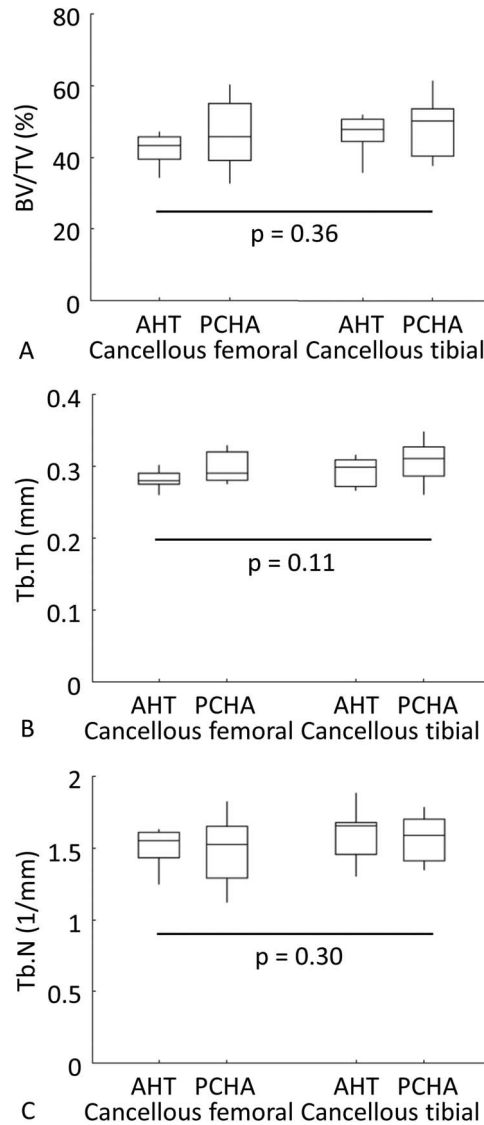


Fig. 11 A-C Descriptive statistics for femoral and tibial (A) bone volume/tissue volume (BV/TV, %), (B) trabecular thickness (Tb.Th, mm), and (C) trabecular number (Tb.N, mm⁻¹) for cancellous bone surrounding AHT and PCHA implants are shown. In the box and whisker plots, the box center line indicates the median value, box limits indicate the first (25th percentile) and third (75th percentile) quartiles, and the whiskers indicate the minimum and maximum values. The p values refer to the results of the corresponding linear mixed model.

evaluation of the alkaline heat-treated surface. For the primary measure of bone-implant osseointegration strength, interfacial shear stress, the AHT surface provided an approximately 35% and 20% improvement at cortical and cancellous bone sites, respectively. This suggests, at minimum, that alkaline heat-treated implants could be used in humans with a reasonable expectation that they would osseointegrate similarly to, or better than, a PCHA equivalent.

The timepoint evaluated (12 weeks) corresponded to the approximate time required to rebuild a structural unit of trabecular osteoid in healthy adult sheep (~80 days) [30], and earlier timepoints representing the healing responses are necessary to assess the acute postoperative response. A long-term study is also required to determine the physiologic local and systemic response to extended implantation with this textured surface.

We assessed only one implant-bone fit for each bone type (cancellous: press-fit; cortical: line-to-line fit). These fits represent the ideal bone-implant contact conditions of orthopaedic screws, pins, and arthroplasty stems; however, unintended gaps may occur at some locations along an arthroplasty stem (for example), and 1- to 2-mm gaps are reported to affect osseointegration of various implant surfaces at early points with this model [12, 87]. Evaluation of the tissue response to alkaline heat-treated surface treatment in the presence of gaps would be needed to determine whether this influenced tissue growth and ingrowth characteristics (such as type, rate, and extent).

For clinical relevance, we compared the novel implant surface with PCHA, which is a gold-standard implant surface with a successful clinical history [6, 28], with the null hypothesis that the AHT surface would show no difference in the defined primary and secondary outcome measures when compared with this gold-standard uncemented surface. Widely used uncemented prosthesis surfaces include hydroxyapatite only, plasma-sprayed, commercially pure titanium (CP Ti), a mixture of these two (PCHA; as used in this study), and sintered beads [54]. No single uncemented surface has demonstrated clinical superiority. Although hydroxyapatite has been included as a constituent of uncemented coatings due to its theoretical ability to increase osseointegration and reduce the likelihood of a fibrous membrane [36], a long-term comparison of two hip stems with identical geometry but with and without hydroxyapatite showed no difference in survivorship [58]. Study logistics meant that it was not possible to evaluate all uncemented surfaces currently in clinical use. The rationale for choosing PCHA among the various uncemented surfaces is so the existing Paragon™ hip (with PCHA coating) can be used as comparator implant versus an alkaline heat-treated version of the Paragon™ hip with identical stem geometry in a subsequent noninferiority clinical study. The results realized in this sheep long bone model form part of an ethical and staged adoption approach to innovation, whereby the results of laboratory and then animal studies justify the progression to limited human trials followed by market release.

The implant was evaluated at both cortical and cancellous bone locations; however, feasible cancellous sites are limited in size, and the implants in the epiphyseal

cancellous bone of the femur and tibia were adjacent to the epiphyseal plate. As such, the implant surface may have had a degree of contact with the reserve zone of the epiphyseal plate, which may have resulted in differing implant integration with bone in those regions. The measures for bone volume and intersection surface may have been affected by this variation in implant positioning.

The evaluation of bone ingrowth and bone architecture adjacent to implants with high radiodensity using micro-CT imaging has limited value. The relatively low resolution and image artefact on the implant surface prevents a detailed view of the contact between bone and implant. A survey of representative implant surfaces by SEM partially overcomes the shortcoming of the quantitative micro-CT analyses by providing observational high-resolution images of bone integration on the implant surface.

Discussion of Key Findings

Biomechanical testing generally favored AHT implants over PCHA Ti implants, with the most consistent differences observed for interfacial shear strength and peak load. These findings, together with the observation that while construct failure occurred at or near the bone-implant interface for both implant types, cancellous AHT implants typically retained a greater amount of bone tissue than cancellous PCHA implants (Supplementary Fig. 7; <http://links.lww.com/CORR/A898>), indicate that osseointegration was stronger for AHT implants. This suggests, within the context of the limitations described, that the alkaline heat-treated surface may promote osseointegration of uncemented orthopaedic implants.

Several other studies have used a similar sheep model with cylindrical dowel implants to evaluate the osseointegration of various surface treatments on titanium alloy substrates over 12 weeks [11-13, 18, 19, 26, 84, 87]. Direct comparison of mechanical parameters derived from push-through tests between studies is cautioned because these measures are likely to be affected by study-specific animal effects, baseline implant surface preparation, implantation conditions, mechanical testing protocols, and data processing procedures. In the current study, the cortical interface shear strength for both the PCHA and AHT surfaces was similar to that of previous studies (Supplementary Table 3; <http://links.lww.com/CORR/A897>). The interface shear strength for titanium alloy dowels with micron-scale machined pillars ranged from 24.1 ± 6.6 MPa to 29.9 ± 6.3 MPa [18, 19]; for hydroxyapatite and vacuum plasma-sprayed titanium, shear strength was 18.9 ± 4.0 MPa and 26.5 ± 3.4 MPa, respectively [87]; and slightly higher results were reported for plasma-sprayed titanium (33 ± 9.5

MPa), plasma-sprayed hydroxyapatite (35.4 ± 8.4 MPa), and anodic spark deposition Ti (33.8 ± 7.8 MPa) [13]. Similar interface shear strength has been reported for sintered titanium beads without (34.5 ± 5.5 MPa) and with (40 ± 6 MPa) hydroxyapatite coating [84], porous titanium alloy (26.1 ± 8.6 MPa [12], plasma-sprayed titanium without (29.0 ± 8.2 MPa) and with (28.3 ± 5.4 MPa) dicalcium phosphate dihydrate coating [26], and plasma-sprayed titanium (24.4 ± 6.8 MPa) and electron beam melting textured titanium (29.8 ± 10.3 MPa) [11]. To our knowledge, there are no reports of shear interface strength for dowels implanted in cancellous bone sites.

In this sheep model, we found that AHT titanium implants offered advantages in terms of cortical osseointegration, as assessed by micro-CT and histomorphometry, compared with conventional PCHA implants. However, in cancellous bone, AHT implants exhibited unchanged bone volume surrounding the implant when compared with the PCHA implants. The bone volume surrounding AHT implants was also comparable with bone volumes in previous studies examining implants of titanium and other materials in the sheep long bone model [18, 65, 82]. This suggests that the line-to-line fit of alkaline heat-treated implants in cortical bone favors osseointegration as measured by micro-CT and histological analyses and is consistent with absence of both fibrous encapsulation and osteolysis of bone surrounding alkaline heat-treated implants. In cancellous bone, it is unclear why the bone volume measures surrounding and in contact with the AHT implants were not associated with the increased interfacial shear stress observed in push-out tests. It is possible that bone integration in the nanotextured surface of the AHT implants contributed to the increased interface strength, which micro-CT and histological analyses were unable to detect. Although intimate interaction of bone mineral with the AHT implant surface was observed by SEM imaging, further studies would be needed to obtain quantitative measures to address this question.

The functional goal of osseointegration is to produce sufficient mechanical coupling between the implant and the surrounding bone to withstand the stresses imparted at the interface by *in vivo* loads. Although *ex vivo* push-through or pull-out tests are commonly used to assess osseointegration, isolating the contribution of the local bone-implant interface mechanics and the contribution of the surrounding bone (the structure and quality of which may also be influenced *in vivo* by the implant characteristics) is challenging. Trabecular bone structure (such as BV/TV) [60], and quality (such as mineral density) [10] surrounding implanted screws likely influences mechanical performance, and fracture initiation can occur within the surrounding bone rather than at the interface (at around 300 to 500 μm around screws in rat

trabecular bone) [59]. The current study did not seek to determine a relationship between the measures derived from micro-CT, histology, and mechanical testing, but it is important to consider that the implant may affect bone distal to the implant interface, and that the mechanical behavior of the construct is likely influenced by both the surface osseointegration and the bone adjacent the interface region.

SEM imaging of explants after mechanical testing revealed that remaining bone integrated intimately with the nanostructured surface. In a recent review, Dobbenga et al. [33] demonstrated that surface topography alterations at the nanolevel can have a notable influence on host cell adhesion, differentiation, and proliferation. Furthermore, the altered chemistry of the alkaline heat-treated surface may be more favorable for bone mineralization [40, 51, 52, 56, 57, 81]. Generally, untreated Ti surfaces consist of a very thin oxide layer, primarily in an amorphous phase. Heat treatments such as that used in the preparation of the AHT implants led to a partial phase transition to the crystalline anatase form of titanium oxide. Sollazzo et al. [78], using a rabbit model, showed that inducing an anatase state on the surface of titanium implants increased bone ongrowth. An anatase phase on the surface of titanium (Ti) can absorb greater amounts of hydroxide and phosphate ions than an amorphous phase [1, 46]. Furthermore, the use of KOH as the etchant leads to the release of K^+ ions from the implant surface into the surrounding body fluid via an ion exchange reaction with H_3O^+ ions, resulting in many Ti-OH groups forming on its surface [56]. These Ti-OH groups initially combine with Ca^{2+} ions to form amorphous calcium titanate in the body environment, and later the calcium titanate combines with phosphate ions to form calcium phosphate and then transforms into bone-like apatite, producing a highly favorable environment for bone ongrowth [56]. Camargo et al. [17] showed that a similar alkaline heat treatment to that used in our study induced apatite formation in simulated body fluid and produced excellent osseointegration *in vivo*. Although it remains challenging to delineate the influence of nanotopographic and chemical alterations caused by such alkaline heat treatments, synergistic effects might contribute to the enhanced osseointegration noted in our study.

Alkaline heat-treated surfaces can be broadly characterized as being subjected to an alkaline etchant such as sodium, potassium, or calcium hydroxide in combination with elevated temperature. Such treatments lead to changes in the nanoarchitecture and surface chemistry. Nanoarchitectural features such as sharpness, height, and spacing of the protrusions are dependent on the cation, the etching time, and the temperature. Although the alkaline heat-treated surface in this study may appear superficially to be similar to other alkaline heat-treated surfaces, the

particular nanoarchitecture employed in the present study was specifically designed to be optimally lethal to clinically relevant bacteria [16].

Conclusion

We have previously shown that a novel, nanostructured surface formed on a titanium alloy via an alkaline heat treatment demonstrated antimicrobial properties. Although this innovation holds the potential to reduce the incidence of periprosthetic joint infection, it is essential to ensure that such a surface modification does not negatively affect osseointegration. Even though it is not possible to conclude that the differences reported herein will be clinically meaningful, the results of this *in vivo* sheep study suggest that the AHT surface provided a stronger bone-implant interface than the PCHA implant at 12 weeks post-implantation in both cortical and cancellous bone. These results provide support for a future clinical noninferiority study comparing PCHA and AHT surfaces on hip stems with identical geometry.

Acknowledgments We thank the scientific and technical assistance of Microscopy Australia at the University of South Australia, Mawson Lakes Campus, a facility that is funded by the university and state and federal governments. We thank the Preclinical, Imaging and Research Laboratories at the South Australian Health and Medical Research Institute and thank the colocated facilities and scientific and technical assistance of the National Imaging Facility, a National Collaborative Research Infrastructure capability. We acknowledge use of facilities in the Solid State and Elemental Analysis Unit at Mark Wainwright Analytical Centre, University of New South Wales. We acknowledge use of the facilities of Adelaide Microscopy, and the Histology and Biomechanics laboratories at the Adelaide Medical School, the University of Adelaide. We thank Jana Bednarz BPsych(Hons), GDip(Biostat) of the University of Adelaide for statistics expertise.

References

- Akin FA, Zreiqat H, Jordan S, Wijesundara MJB, Hanley L. Preparation and analysis of macroporous TiO₂ films on Ti surfaces for bone-tissue implants. *J Biomed Mater Res*. 2001;57:588-596.
- Arens D, Sigrist I, Alini M, et al. Seasonal changes in bone metabolism in sheep. *Vet J*. 2007;174:585-591.
- ASTM International. Standard specification for titanium and titanium-6 aluminum-4 vanadium alloy powders for coatings of surgical implants. ASTM standard F1580-12. *Annual Book of ASTM Standards*. ASTM International; 2012. DOI: 10.1155/2011/836587.
- ASTM International. Standard specification for wrought titanium-6 aluminum-4 vanadium ELI (extra low interstitial) alloy for surgical implant applications (UNS R56401). ASTM standard F136-13. *Annual Book of ASTM Standards*. ASTM International; 2013. DOI: 10.1520/F0136-13.
- ASTM International. Standard specification for composition of hydroxylapatite for surgical implants. ASTM standard F1185-03. *Annual Book of ASTM Standards*. ASTM International; 2014. DOI: 10.1520/F1185-03R14.
- Australian Orthopaedic Association National Joint Replacement Registry. Hip, knee & shoulder arthroplasty. 2021 annual report. Available at: <https://aoanjrr.sahmri.com/documents/10180/712282/Hip%2C+Knee+%26+Shoulder+Arthroplasty>. Accessed March 23, 2022.
- Babuska V, Moztarzadeh O, Kubikova T, et al. Evaluating the osseointegration of nanostructured titanium implants in animal models: current experimental methods and perspectives (review). *Biointerphases*. 2016;11:030801.
- Bansal R, Singh JK, Singh V, Singh DDN, Das P. Optimization of oxidation temperature for commercially pure titanium to achieve improved corrosion resistance. *J Mater Eng Perform*. 2017;26:969-977.
- Behery OA, Kearns SM, Rabinowitz JM, Levine BR. Cementless vs cemented tibial fixation in primary total knee arthroplasty. *J Arthroplasty*. 2017;32:1510-1515.
- Bernhardsson M, Sandberg O, Aspenberg P. Experimental models for cancellous bone healing in the rat comparison of drill holes and implanted screws. *Acta Orthop*. 2015;86:745-750.
- Bertollo N, Da Assuncao R, Hancock NJ, Lau A, Walsh WR. Influence of electron beam melting manufactured implants on ingrowth and shear strength in an ovine model. *J Arthroplasty*. 2012;27:1429-1436.
- Bertollo N, Matsubara M, Shinoda T, et al. Effect of surgical fit on integration of cancellous bone and implant cortical bone shear strength for a porous titanium. *J Arthroplasty*. 2011;26:1000-1007.
- Bertollo N, Sandrini E, Dalla Pria P, Walsh WR. Osseointegration of multiphase anodic spark deposition treated porous titanium implants in an ovine model. *J Arthroplasty*. 2015;30:484-488.
- Bhadra CM, Truong VK, Pham VTH, et al. Antibacterial titanium nano-patterned arrays inspired by dragonfly wings. *Sci Rep*. 2015;5:16817.
- Bright R, Fernandes D, Wood J, et al. Long-term antibacterial properties of a nanostructured titanium alloy surface: an *in vitro* study. *Mater Today Bio*. 2022;13:100176.
- Bright R, Hayles A, Fernandes D, et al. *In vitro* bactericidal efficacy of nanostructured Ti6Al4V surfaces is bacterial load dependent. *ACS Appl Mater Interfaces*. 2021;13:38007-38017.
- Camargo WA, Takemoto S, Hoekstra JW, et al. Effect of surface alkali-based treatment of titanium implants on ability to promote *in vitro* mineralization and *in vivo* bone formation. *Acta Biomater*. 2017;57:511-523.
- Causesy GC, Picha GJ, Price J, et al. The effect of a novel pillar surface morphology and material composition demonstrates uniform osseointegration. *J Mech Behav Biomed*. 2021; 123:104775.
- Causesy GC, Picha GJ, Price J, et al. *In-vivo* response to a novel pillared surface morphology for osseointegration in an ovine model. *J Mech Behav Biomed*. 2021;119:104462.
- Chavassieux P. Bone effects of fluoride in animal models *in vivo*. A review and a recent study. *J Bone Miner Res*. 1990;5(suppl 1): S95-99.
- Chavassieux P, Buffet A, Vergnaud P, Garnero P, Meunier PJ. Short-term effects of corticosteroids on trabecular bone remodeling in old ewes. *Bone*. 1997;20:451-455.
- Chavassieux P, Garnero P, Dubouef F, et al. Effects of a new selective estrogen receptor modulator (MDL 103,323) on cancellous and cortical bone in ovariectomized ewes: a biochemical, histomorphometric, and densitometric study. *J Bone Miner Res*. 2001;16:89-96.
- Chavassieux P, Pastoureaux P, Boivin G, Chapuy MC, Delmas PD, Meunier PJ. Dose effects on ewe bone remodeling of short-

- term sodium fluoride administration—a histomorphometric and biochemical study. *Bone*. 1991;12:421-427.
24. Chavassieux P, Pastoureaux P, Boivin G, et al. Fluoride-induced bone changes in lambs during and after exposure to sodium fluoride. *Osteoporos Int*. 1991;2:26-33.
 25. Chavassieux P, Pastoureaux P, Chapuy MC, Delmas PD, Meunier PJ. Glucocorticoid-induced inhibition of osteoblastic bone formation in ewes: a biochemical and histomorphometric study. *Osteoporos Int*. 1993;3:97-102.
 26. Chen D, Bertollo N, Lau A, et al. Osseointegration of porous titanium implants with and without electrochemically deposited DCPS coating in an ovine model. *J Orthop Surg Res*. 2011;6:56.
 27. Christou C, Oliver RA, Rawlinson J, Walsh WR. Transdermal fentanyl and its use in ovine surgery. *Res Vet Sci*. 2015;100:252-256.
 28. Coffey SP, Sorial RM, Sharma R, Field JR. Two-year migration characteristics of a novel cementless femoral stem: a radio-stereometric analysis and clinical outcomes study. *ANZ J Surg*. 2021;91:398-403.
 29. Collier JP, Surprenant VA, Mayor MB, et al. Loss of hydroxyapatite coating on retrieved, total hip components. *J Arthroplasty*. 1993;8:389-393.
 30. Delmas PD, Vergnaud P, Arlot ME, Pastoreau P, Meunier PJ, Nilsson MH. The anabolic effect of human PTH (1-34) on bone formation is blunted when bone resorption is inhibited by the bisphosphonate tiludronate—is activated resorption a prerequisite for the in vivo effect of PTH on formation in a remodeling system? *Bone*. 1995;16:603-610.
 31. Dempster DW, Compston JE, Drezner MK, et al. Standardized nomenclature, symbols, and units for bone histomorphometry: a 2012 update of the report of the ASBMR histomorphometry nomenclature committee. *J Bone Miner Res*. 2013;28:2-17.
 32. Dhert WJ, Verheyen CC, Braak LH, et al. A finite element analysis of the push-out test: influence of test conditions. *J Biomed Mater Res*. 1992;26:119-130.
 33. Dobbenga S, Fratila-Apachitei LE, Zadpoor AA. Nanopattern-induced osteogenic differentiation of stem cells - a systematic review. *Acta Biomater*. 2016;46:3-14.
 34. Elias CN, Lima JHC, Valiev R, Meyers MA. Biomedical applications of titanium and its alloys. *JOM*. 2008;60:46-49.
 35. Elliott B, Goswami T. Implant material properties and their role in micromotion and failure in total hip arthroplasty. *Int J Mech Mater Des*. 2012;8:1-7.
 36. Epinette JA, Manley MT. Uncemented stems in hip replacement - hydroxyapatite or plain porous: does it matter? Based on a prospective study of HA Omnifit stems at 15-years minimum follow-up. *Hip Int*. 2008;18:69-74.
 37. Faul F, Erdfelder E, Lang AG, Buchner A. G*power 3: a flexible statistical power analysis program for the social, behavioral, and biomedical sciences. *Behav Res Methods*. 2007;39:175-191.
 38. Giavaresi G, Giardino R, Ambrosio L, et al. In vitro biocompatibility of titanium oxide for prosthetic devices nanostructured by low pressure metal-organic chemical vapor deposition. *Int J Artif Organs*. 2003;26:774-780.
 39. Gruner H. Titanium in medicine: material science, surface science, engineering, biological responses, and medical applications. In: Brunette DM, ed. *Engineering Materials*. Springer; 2001:375-416.
 40. Guo ZJ, Jiang N, Chen C, et al. Surface bioactivation through the nanostructured layer on titanium modified by facile HPT treatment. *Sci Rep*. 2017;7:4155.
 41. Gupta R, Kumar A. Bioactive materials for biomedical applications using sol-gel technology. *Biomed Mater*. 2008;3:034005.
 42. Hacking SA, Harvey EJ, Tanzer M, Krygier JJ, Bohn JD. Acid-etched microtexture for enhancement of bone growth into porous-coated implants. *J Bone Joint Surg Br*. 2003;85:1182-1189.
 43. Hayles A, Hasan J, Bright R, et al. Hydrothermally etched titanium: a review on a promising mechano-bactericidal surface for implant applications. *Mater Today Chem*. 2021;22:100622.
 44. Hofmann AA, Bloebaum RD, Bachus KN. Progression of human bone ingrowth into porous-coated implants - rate of bone ingrowth in humans. *Acta Orthop Scand*. 1997;68:161-166.
 45. Huracek J, Spirig P. The effect of hydroxyapatite coating on the fixation of hip prostheses - a comparison of clinical and radiographic results of hip-replacement in a matched-pair study. *Arch Orthop Traum Surg*. 1994;113:72-77.
 46. Ishizawa H, Ogino M. Hydrothermal precipitation of hydroxyapatite on anodic titanium oxide films containing CA and P. *J Mater Sci*. 1999;34:5893-5898.
 47. Izmir M, Ercan B. Anodization of titanium alloys for orthopedic applications. *Front Chem Sci Eng*. 2019;13:28-45.
 48. Jäger M, Jennissen HP, Dittrich F, Fischer A, Kohling HL. Antimicrobial and osseointegration properties of nanostructured titanium orthopaedic implants. *Materials*. 2017;10:1302.
 49. Jaggessar A, Mathew A, Wang HX, et al. Mechanical, bactericidal and osteogenic behaviours of hydrothermally synthesised TiO₂ nanowire arrays. *J Mech Behav Biomed*. 2018;80:311-319.
 50. Jordan LR, Olivo JL, Voorhost PE. Survivorship analysis of cementless meniscal bearing total knee arthroplasty. *Clin Orthop Relat Res*. 1997;338:119-123.
 51. Kapadia BH, Berg RA, Daley JA, et al. Periprosthetic joint infection. *Lancet*. 2016;387:386-394.
 52. Kapat K, Maity PP, Rameshbabu AP, et al. Simultaneous hydrothermal bioactivation with nano-topographic modulation of porous titanium alloys towards enhanced osteogenic and antimicrobial responses. *J Mater Chem B*. 2018;6:2877-2893.
 53. Kawanabe K, Ise K, Goto K, et al. A new cementless total hip arthroplasty with bioactive titanium porous-coating by alkaline and heat treatment: average 4.8-year results. *J Biomed Mater Res B*. 2009;90:476-481.
 54. Khanuja HS, Vakil JJ, Goddard MS, Mont MA. Cementless femoral fixation in total hip arthroplasty. *J Bone Joint Surg Am*. 2011;93:500-509.
 55. Kim YH. Long-term results of the cementless porous-coated anatomic total hip prosthesis. *J Bone Joint Surg Br*. 2005;87:623-627.
 56. Kokubo T, Kim HM, Kawashita M, Nakamura T. Bioactive metals: preparation and properties. *J Mater Sci Mater Med*. 2004;15:99-107.
 57. Kokubo T, Yamaguchi S. Novel bioactive titanate layers formed on Ti metal and its alloys by chemical treatments. *Materials*. 2010;3:48-63.
 58. Lazarinis S, Karrholm J, Hailer NP. Effects of hydroxyapatite coating on survival of an uncemented femoral stem a Swedish hip arthroplasty register study on 4,772 hips. *Acta Orthop*. 2011;82:399-404.
 59. Le Cann S, Tudisco E, Tagil M, Hall SA, Isaksson H. Bone damage evolution around integrated metal screws using x-ray tomography - in situ pullout and digital volume correlation. *Front Bioeng Biotechnol*. 2020;8:934.
 60. Le Cann S, Tudisco E, Turunen MJ, et al. Investigating the mechanical characteristics of bone-metal implant interface using in situ synchrotron tomographic imaging. *Front Bioeng Biotechnol*. 2019;6:208.

61. Lopez-Heredia MA, Weiss P, Layrolle P. An electrodeposition method of calcium phosphate coatings on titanium alloy. *J Mater Sci Mater Med*. 2007;18:381-390.
62. Lopez-Valverde N, Lopez-Valverde A, Aragonese JM, et al. Systematic review and meta-analysis of the effectiveness of calcium-phosphate coating on the osseointegration of titanium implants. *Materials (Basel)*. 2021;14:3015.
63. Maher S, Wijenayaka AR, Lima-Marques L, et al. Advancing of additive-manufactured titanium implants with bioinspired micro- to nanotopographies. *ACS Biomater Sci Eng*. 2021;7:441-450.
64. Martini L, Fini M, Giavaresi G, Giardino R. Sheep model in orthopedic research: a literature review. *Comparative Med*. 2001;51:292-299.
65. Meers CMF, Verleye GBM, Smeets D, et al. Fine grained osseointegrative coating improves biocompatibility of peek in heterotopic sheep model. *Int J Spine Surg*. 2015;9:35.
66. Muschler GF, Raut VP, Patterson TE, Wenke JC, Hollinger JO. The design and use of animal models for translational research in bone tissue engineering and regenerative medicine. *Tissue Eng Part B Rev*. 2010;16:123-145.
67. National Health and Medical Research Council. *Australian Code for the Care and Use of Animals for Scientific Purposes*. 8th ed. National Health and Medical Research Council; 2013.
68. Niinomi M, Nakai M. Titanium-based biomaterials for preventing stress shielding between implant devices and bone. *Int J Biomater*. Published online June 22, 2011. DOI: [10.1155/2011/836587](https://doi.org/10.1155/2011/836587).
69. Nunamaker DM. Experimental models of fracture repair. *Clin Orthop Relat Res*. 1998;355(suppl):S56-65.
70. O'Loughlin PF, Morr S, Bogunovic L, et al. Selection and development of preclinical models in fracture-healing research. *J Bone Joint Surg Am*. 2008;90(suppl 1):79-84.
71. Pearce AI, Richards RG, Milz S, Schneider E, Pearce SG. Animal models for implant biomaterial research in bone: a review. *Eur Cells Mater*. 2007;13:1-10.
72. Pulido L, Ghanem E, Joshi A, Purtill JJ, Parvizi J. Periprosthetic joint infection: the incidence, timing, and predisposing factors. *Clin Orthop Relat Res*. 2008;466:1710-1715.
73. Rueden CT, Schindelin J, Hiner MC, et al. ImageJ2: ImageJ for the next generation of scientific image data. *BMC Bioinformatics*. 2017;18:529.
74. Sidambe AT. Biocompatibility of advanced manufactured titanium implants-a review. *Materials (Basel)*. 2014;7:8168-8188.
75. Sittig C, Textor M, Spencer ND, Wieland M, Vallotton PH. Surface characterization of implant materials cp Ti, Ti-6Al-7Nb and Ti-6Al-4V with different pretreatments. *J Mater Sci Mater Med*. 1999;10:35-46.
76. Soballe K, Hansen ES, Brockstedtrasmussen H, Bunger C. Hydroxyapatite coating converts fibrous tissue to bone around loaded implants. *J Bone Joint Surg Br*. 1993;75:270-278.
77. Soballe K, Overgaard S. The current status of hydroxyapatite coating of prostheses. *J Bone Joint Surg Br*. 1996;78:689-691.
78. Sollazzo V, Pezzetti F, Scarano A, et al. Anatase coating improves implant osseointegration in vivo. *J Craniofac Surg*. 2007;18:806-810.
79. Song WH, Jun YK, Han Y, Hong SH. Biomimetic apatite coatings on micro-arc oxidized titania. *Biomaterials*. 2004;25:3341-3349.
80. Souza JCM, Sordi MB, Kanazawa M, et al. Nano-scale modification of titanium implant surfaces to enhance osseointegration. *Acta Biomater*. 2019;94:112-131.
81. Srivas PK, Kapat K, Das B, Pal P, Guha Ray P, Dhara S. Hierarchical surface morphology on Ti6Al4V via patterning and hydrothermal treatment towards improving cellular response. *Appl Surf Sci*. 2019;478:806-817.
82. Svehla M, Morberg P, Bruce W, Walsh WR. No effect of a type I collagen gel coating in uncemented implant fixation. *J Biomed Mater Res B Appl Biomater*. 2005;74:423-428.
83. Svehla M, Morberg P, Bruce W, Zicat B, Walsh WR. The effect of substrate roughness and hydroxyapatite coating thickness on implant shear strength. *J Arthroplasty*. 2002;17:304-311.
84. Svehla M, Morberg P, Zicat B, et al. Morphometric and mechanical evaluation of titanium implant integration: comparison of five surface structures. *J Biomed Mater Res*. 2000;51:15-22.
85. Swarts E, Bucher TA, Phillips M, Yap FH. Does the ingrowth surface make a difference? A retrieval study of 423 cementless acetabular components. *J Arthroplasty*. 2015;30:706-712.
86. Tonino AJ, Therin M, Doyle C. Hydroxyapatite-coated femoral stems. Histology and histomorphometry around five components retrieved at post mortem. *J Bone Joint Surg Br*. 1999;81:148-154.
87. Walsh WR, Pelletier MH, Bertollo N, et al. Bone ongrowth and mechanical fixation of implants in cortical and cancellous bone. *J Orthop Surg Res*. 2020;15:177.
88. Walsh WR, Pelletier MH, Christou C, et al. The in vivo response to a novel Ti coating compared with polyether ether ketone: evaluation of the periphery and inner surfaces of an implant. *Spine J*. 2018;18:1231-1240.
89. Walsh WR, Pelletier MH, Wang T, et al. Does implantation site influence bone ingrowth into 3D-printed porous implants? *Spine J*. 2019;19:1885-1898.
90. Willie BM, Bloebaum RD, Bireley WR, Bachus KN, Hofmann AA. Determining relevance of a weight-bearing ovine model for bone ingrowth assessment. *J Biomed Mater Res A*. 2004;69:567-576.
91. Xiao M, Chen YM, Biao MN, Zhang XD, Yang BC. Bio-functionalization of biomedical metals. *Mat Sci Eng C Mater Biol Appl*. 2017;70:1057-1070.
92. Yoda I, Koseki H, Tomita M, et al. Effect of surface roughness of biomaterials on Staphylococcus epidermidis adhesion. *BMC Microbiol*. 2014;14:234.
93. Zarrinkalam MR, Beard H, Schultz CG, Moore RJ. Validation of the sheep as a large animal model for the study of vertebral osteoporosis. *Eur Spine J*. 2009;18:244-253.
94. Zhu CY, Lv YT, Qian C, et al. Proliferation and osteogenic differentiation of rat BMSCs on a novel Ti/SiC metal matrix nanocomposite modified by friction stir processing. *Sci Rep*. 2016;6:38875.